Electrochimica Acta 147 (2014) 241–249

Contents lists available at ScienceDirect

Electrochimica Acta

journal homepage: www.elsevier.com/locate/electacta

Improved Lithium Ion Behavior Properties of TiO_2@Graphitic-like Carbon Core@Shell Nanostructure

Min-Cheol Kim [a,1], Young-Woo Lee [a,1], Si-Jin Kim [a], Bo-Mi Hwang [a], Han-Chul Park [a], Eui-Tak Hwang [a], Guozhong Cao [b], Kyung-Won Park [a,*]

[a] *Department of Chemical Engineering, Soongsil University, Seoul 156743, Republic of Korea*
[b] *Department of Materials Science and Engineering, University of Washington, Seattle, WA 98195, USA*

ARTICLE INFO

Article history:
Received 28 August 2014
Received in revised form 20 September 2014
Accepted 24 September 2014
Available online 28 September 2014

Keywords:
TiO_2
Intercalation
Electrochemistry
Capacitance
Lithium Ion batteries

ABSTRACT

We demonstrate TiO_2@graphitic-like carbon core@shell (TiO_2@C) nanostructures using chemical vapor deposition as the heating process under a CH_4 atmosphere at 700 °C (TiO_2@C-700). The TiO_2@C-700 nanostructure consists of a TiO_2 core coated by a carbon shell. The carbon shells on TiO_2 nanostructures generally have 2∼3 layers exhibiting graphitic-like properties. The TiO_2@C-700 nanostructure is homogeneously covered with a graphite-like carbon layer, resulting in excellent contact between the TiO_2 and carbon and improving the electrical conductivity. The improved specific capacity and electrochemical properties of the TiO_2@C-700 nanostructure are attributed to the graphitic-like carbon acting as a conductive region, resulting in improved electron transport properties on the electrode surface and enhanced lithium ion intercalation, leading to lower charge transfer resistance and high diffusion coefficient. The combination of electrochemical data and structural properties of the TiO_2@C-700 nanostructure makes it a promising candidate for the anode in lithium ion batteries.

1. Introduction

Lithium ion batteries (LIBs) are excellent power sources for portable and transportation applications, because of their relatively high energy density, high voltage, high power density, long operating life, etc [1–4]. In LIBs, the cathodes consist of transition metal oxide containing lithium sources (e.g., $LiCoO_2$, $LiMn_2O_4$, and $LiMnPO_4$, etc.), which typically show a higher voltage and lower capacity than the anodes [5–7]. On the other hand, the anodes mainly utilize carbon-based materials (e.g., carbon black, carbon nanotube, carbon nanofiber, and graphene) having a higher conductivity and initial capacitance, and typically show a lower voltage and higher capacity than the cathodes [8–10]. Besides, in the anodes, transition metal oxides have been utilized due to their low cost, good safety features, environmental friendliness, and especially their high lithium intercalation potential in comparison with carbon-based materials [11–13]. Among the transition metal oxides, TiO_2 is regarded as a promising lithium ion insertion/desertion material with a low production cost, high abundance, non-toxicity, very low volume change during lithium ion insertion/desertion (3–4%), good structural stability, and long cycle life [14–17]. However, TiO_2 has limitations such as a lower initial-practical capacity than the theoretical value (335 mAh g^{-1}) and low high-rate capability, due to its poor ionic conductivity and electrical conductivity [18–20]. There have been many reports in the literature on the improvement of the electrochemical properties by structure-controlled or complex nanostructures.

Structure-controlled TiO_2 nanostructures show improved lithium ion intercalation properties due to their large specific surface area or short transport distance [21–23]. Also, complex nanostructures show improved electrical conductivity or pseudo-capacitive contribution due to the formation of a complex with the carbon-based materials or conducting polymers (e.g., polyaniline and polypyrrole, etc.) [24–26]. However, the above approaches have several problems such as the non-homogeneity of the composition in the complex nanostructures and low composition yield during the synthesis process. In order for them to have excellent electrochemical properties, the TiO_2-based nanostructures employed as the anode must consist of nanocrystalline structures having a uniform size and homogeneous composition in the complex nanostructures, as well as an increased number of active sites for lithium ion insertion/desertion [27–29].

In this work, the use of a TiO_2@graphitic-like carbon nanostructure was investigated as a possible anodic material for LIBs. As shown in Fig. 1, the TiO_2 nanostructure has active sites for

---

[*] Corresponding author. Tel.: +82 2 820 0613; fax: +82 2 812 5378.
E-mail address: kwpark@ssu.ac.kr (K.-W. Park).
[1] These authors contributed equally.

http://dx.doi.org/10.1016/j.electacta.2014.09.114
0013-4686/© 2014 Published by Elsevier Ltd.

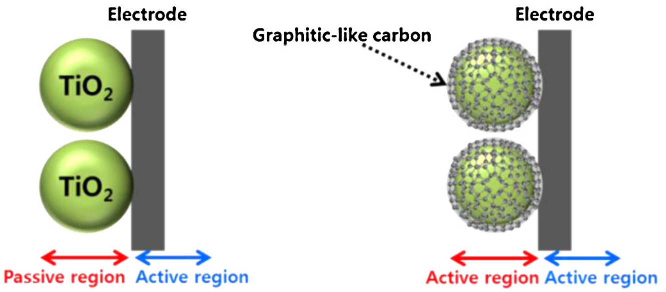

Fig. 1. Relationship between the electrical characteristics of the fresh TiO_2 and TiO_2@C-700 nanostructure.

the lithium ion insertion/desertion reaction. This leads to a low capacity at high rates and high interface resistance. Meanwhile, the TiO_2@graphitic-like carbon nanostructure has active sites and an active region, leading to higher electrical conductivity, high capacitance at high rates and enhanced pseudocapacitive properties. The main objectives of this study were to investigate: a) the conductivity change resulting from the graphitic-like carbon shell and b) the high-rate performance of lithium ion insertion/desertion, cyclability, and interface capacitance afforded by the TiO_2@graphitic-like carbon nanostructure as compared to that of the fresh TiO_2 nanostructure.

Herein, we suggest the use of a complex nanostructure consisting of a TiO_2 core and graphitic-like carbon shell as the anodic materials for LIBs. The TiO_2@C nanostructure consists of TiO_2 with a carbon shell formed by heat treatment of TiO_2 at 700 °C in CH_4. The morphology and structure of the as-prepared nanostructures were characterized using field-emission transmission electron microscopy (FE-TEM), X-ray diffraction (XRD), and Raman spectroscopy. The chemical properties of the as-prepared nanostructures were characterized using X-ray photo-electron spectroscopy (XPS) and thermogravimetric analysis (TGA). To evaluate their performance in LIBs, the charge-discharge and high-rate curves, cyclic voltammograms (CVs), and electrochemical impedance spectroscopy (EIS) spectra of the electrodes were measured using a lithium coin cell.

2. Experimental

2.1. Synthesis of the TiO_2@C nanostructures.

The nanostructures consisting of a TiO_2 core and carbon shell used commercial TiO_2 (Degussa, P-25) as the starting material and were prepared by means of heat treatment under a CH_4 atmosphere at 700 °C. The TiO_2 powders (0.2 g) were put into a quartz boat which was placed in a quartz tube system under a flow of CH_4 gas. First, a flow of N_2 gas was maintained for 15 min to get rid of the air inside the tube. Then, under a CH_4 flow rate of 100 mL min^{-1}, the furnace was heated from room temperature to 700 °C and then maintained at this temperature for 3 h. After the heat treatment for 3 h, the furnace was cooled down to room temperature under a methane gas atmosphere. Also, for comparison with the TiO_2@C-700 sample, an annealed TiO_2 sample (TiO_2-700) was prepared by means of heat treatment at 700 °C for 3 h under an air atmosphere.

2.2. Structural analysis.

The TiO_2@C-700 and TiO_2-700 nanostructures were characterized by FE-TEM using a Philips Tecnai F20 electron microscope system at 200 kV and FEI company Tecnai G2 F30 electron microscope system at 300 kV. The FE-TEM samples were prepared by placing a drop of the catalyst suspension with ethanol on a copper grid. Structural analysis of the samples was carried out using a Rigaku diffractometer equipped with a Cu K_α radiation source of $\lambda = 0.15418$ nm with a Ni filter. The tube current was 100 mA with a tube voltage of 40 kV. 2θ values between 20 and 60° were explored at a scan rate of 4° min^{-1}. Raman spectra were recorded on a high resolution Micro-Raman spectrometer (LabRAM HR UV/Vis/NIR PL) using an Ar ion laser with $\lambda = 514.5$ nm. XPS (Thermo Scientific, K-Alpha) analysis was carried out with an Al Kα X-ray source of 1486.8 eV at a chamber pressure below 1×10^{-8} Torr and beam power of 200 W. All of the high resolution spectra were collected using a pass energy of 46.95 eV. The step size and time per step were chosen to be 0.025 eV and 100 ms, respectively. Both ends of the baseline were set sufficiently far, so as not to distort the shape of the spectra, including their tails. A small variation of the range of the baseline did not affect the relative amount of fitted species (less than 1%). The C 1s electron binding energy was referenced at 284.6 eV and a nonlinear least-squares curve-fitting program was employed with a Gaussian–Lorentzian production function. TGA curves were obtained in a thermal analyzer (SDT Q-600, TA Instruments) in the range of 25–800 °C at a heating rate of 10 °C min^{-1} in an air flow of 60 cm^3 min^{-1}. Also, the electrical conductivity was calculated by equation (1):

$$\sigma = 1/\rho = 1/RA \quad (1)$$

where σ is the electrical conductivity (Siemens, S cm^{-1}), ρ is the specific resistance, l is the thickness of the pellet, R is the resistance, and A is the area of the pellet.

2.3. Preparation of the anodes for electrochemical estimation in LIBs.

The anodes for the LIBs were prepared by mixing 70 wt.% TiO_2@C-700 or TiO_2-700 as the active material, 10 wt.% carbon black (Ketjan Black) as a conducting agent, and 20 wt.% polyvinylidene fluoride (PVDF) as a binder. In order to obtain the slurry, several drops of *N*-methyl-pyrrolidone (NMP) were added to the mixture of the as-prepared nanostructures with carbon black and PVDF. The prepared slurry was homogenized by stirring and then coated uniformly on 15 μm thick copper foil substrates. The electrode with an area of 1.3273 cm^2 was dried in a vacuum oven at 110 °C. The cells were assembled in a high purity argon filled glove box (< 5 ppm, H_2O and O_2) using the TiO_2@C-700 and TiO_2-700 nanostructures as the working electrode, lithium foil (FMC Co.) as the counter electrode and a separator that was saturated with an electrolyte solution consisting of 1.1 M $LiPF_6$ dissolved in a solvent mixture (Techno Semichem Co.) of ethylene carbonate (EC) and di-methyl carbonate (DMC) with a volume ratio of EC/DMC = 1:1.

2.4. Electrochemical measurement.

The electrochemical properties of the assembled cells were recorded with charge/discharge curves in the voltage window between 1.0 and 3.0 V (V *vs.* Li/Li^+). The charge/discharge tests were galvanostatically cycled between 1.0 and 3.0 V (V *vs.* Li/Li^+) for 40 cycles at a current rate of 0.2 C. All of the electrochemical measurements were carried out at 25 °C. For the EIS analysis, the excitation potential applied to the cells was 5 mV in the frequency range between 100 kHz and 0.01 Hz at full charge. The CVs of the electrodes were measured at different scan rates between 1 and 3 V (V *vs.* Li/Li^+) using a potentiostat (Eco Chemie, AUTOLAB). To estimate the capacitance of the electrodes, the CVs were measured in a three-electrode cell at different scan rates between 0 and 1 V (V *vs.* Ag/AgCl) in 0.5 M H_2SO_4 solution using a potentiostat.

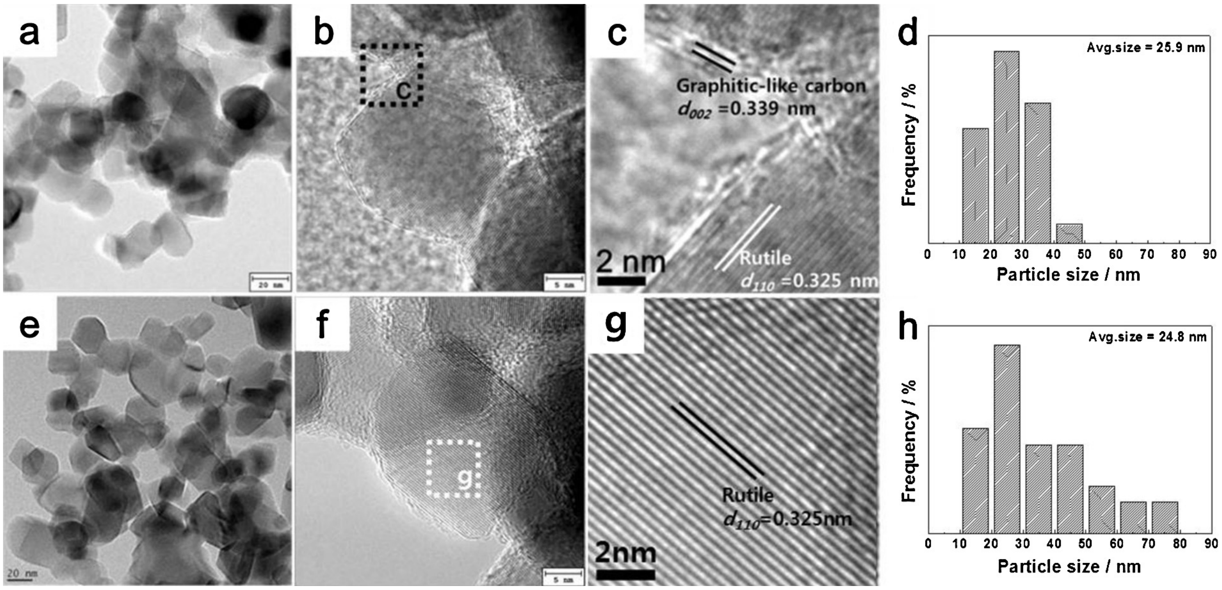

Fig. 2. (a) FE-TEM and (b) HR-TEM images of the TiO_2@C-700 nanostructure. (c) HR-TEM image of the TiO_2@C-700 nanostructure containing {002} facet of graphitic-like carbon and {110} facet of rutile phase. (d) Particle size distribution histogram of the TiO_2@C-700 nanostructure. (e) FE-TEM and (f) HR-TEM images of the TiO_2-700 nanostructure. (g) HR-TEM image of the TiO_2-700 nanostructure containing {101} facet of anatase phase. (h) Particle size distribution histogram of the TiO_2-700 nanostructure.

3. Results and discussion

Fig. 2(a)-(c) shows the TEM images of the TiO_2 nanostructures heated at 700 °C in a CH_4 gas atmosphere. As shown in Fig. 2(a and b), the carbon-shell structures were homogeneously coated on the surface of the TiO_2 nanoparticles. The TiO_2 core material of the TiO_2@C-700 nanostructure consists of the {110} facet with a *d*-spacing of 0.325 nm in the TiO_2 rutile phase, whereas the carbon shell material consists of the {002} facet with a *d*-spacing of 0.339 nm in the graphitic layers, as shown in the HR-TEM image of Fig. 2(c), which is similar to the {002} facet with *d*-spacing of 0.335 nm of typical graphite. It is evident that the TiO_2@C-700 nanostructure consists of a TiO_2 core coated with a graphitic-like carbon shell. Furthermore, the graphitic-like carbon shells on TiO_2 generally consist of 2∼3 layers. The graphitic-like carbon layers are formed by the heat treatment process under a CH_4 atmosphere. The formation of the TiO_2@C nanostructure may take place according to equation (2) [30]:

$$TiO_2 + CH_4 \rightarrow iO_2 + C_{ad} + 2H_2 \rightarrow TiO_2@C\ (2) \qquad (2)$$

Fig. 2(e)-(g) shows the TEM images of the TiO_2 samples heated at 700 °C for 3 h in an air atmosphere. The TiO_2-700 nanostructure consists of the {101} facet with a *d*-spacing of 0.352 nm in the TiO_2 anatase phase, as shown in the high-resolution TEM (HR-TEM) image of Fig. 2(g). The average particle sizes of the TiO_2@C-700 and TiO_2-700 nanostructures in Fig. 2(d) and (h) are 25.9 ± 7.4 and 24.8 ± 10.2 nm, respectively. In particular, the average particle size of the TiO_2-700 nanostructure is similar to that of the TiO_2@C-700 nanostructure including the carbon layers (3–4 nm), but the particle distribution of the former is wider than that of the latter. This explains why the formation of the carbon shell during the heat treatment process of the TiO_2@C-700 nanostructure prevents the aggregation of the TiO_2 nanoparticles. Thus, the TiO_2@C-700 nanostructure may have a homogeneous graphitic-like carbon shell and uniform particle size of TiO_2.

Fig. 3 shows the XRD patterns of the TiO_2@C-700, TiO_2-700, and TiO_2 in comparison with the XRD reference data of TiO_2 anatase and rutile phases. Typically, commercial TiO_2 consists of dominant anatase and rutile phases of TiO_2, as indicated in Fig. 3(a), and shows an intensity ratio of the (101) plane of the anatase phase to the (110) plane of the rutile phase of 5.9. In contrast, the annealed TiO_2 samples (e.g., TiO_2@C-700 and TiO_2-700) display a mixture of anatase and rutile phases of TiO_2, with rutile being dominant, which means that the phase transformation of anatase into rutile phase takes place during the heat treatment process, as shown in Fig. 3(b) and (c). It is observed that the anatase phase is transformed into the rutile phase in CH_4 and air atmospheres. In general, it is known that the phase transformation from metastable anatase to stable rutile occurs at around 600 °C [31].

Fig. 4shows the XPS spectra of the individual curves of Ti 2p, O 1s, and C 1s measured at high resolution on the TiO_2@C-700 and TiO_2-700 nanostructures. As shown in Fig. 4(a), the Ti $2p_{3/2}$ and $2p_{1/2}$ peaks of TiO_2@C-700 nanostructure appear at ∼458.9 and ∼464.6 eV, respectively. On the other hand, the Ti $2p_{3/2}$ and $2p_{1/2}$

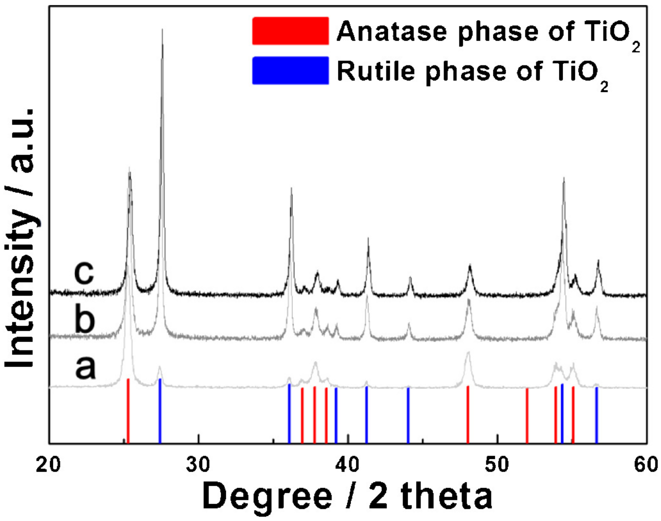

Fig. 3. Wide-range XRD patterns of (a) commercial TiO_2, (b) TiO_2-700, and (c) TiO_2@C-700 in comparison with XRD reference data of anatase phase (red, JCPDS No. 89–4921) and rutile phase (blue, JCPDS No. 89–4920) of TiO_2.

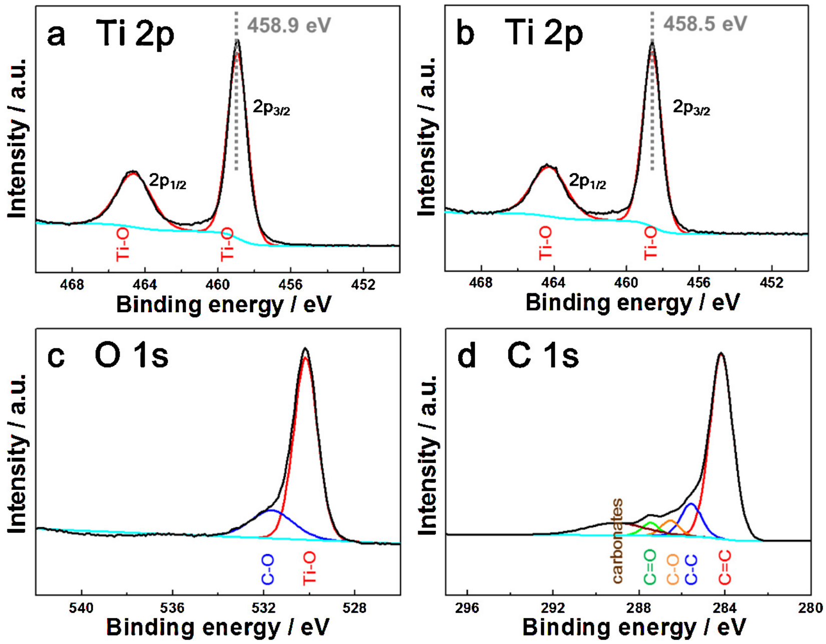

Fig. 4. Ti 2p XPS spectra of (a) TiO_2@C-700 and (b) TiO_2-700 nanostructures. (c) O 1s and (d) C 1s spectra of TiO_2@C-700

peaks of TiO_2-700 nanostructure appear at ~458.5 and ~464.2 eV, respectively, in Fig. 4(b). The Ti 2p peaks of TiO_2@C-700 nanostructure appear slightly negative shifting toward higher binding energy in comparison with TiO_2-700 nanostructure, suggesting a strong interaction between TiO_2 as a core and graphitic-like carbon as a shell [32]. The XPS spectrum of O 1 s of TiO_2@C-700 nanostructure consists of two peaks in Fig. 4(c). The main peak with a binding energy of ~530.2 eV is attributed to the Ti-O bond of the TiO_2 crystal structure, and the positive peak at ~531.6 eV is attributed to the C-O bond, which acts as the binding bond between the TiO_2 core and graphitic-like carbon shell. Meanwhile, the C 1 s spectrum of the TiO_2@C-700 nanostructure includes five peaks, as shown in Fig. 4(d). The peaks at ~284.1, ~285.6, ~286.6, ~287.5, and ~289.1 eV correspond to the C&9552;C bond of the sp^2-hybridized graphitic carbon, C-C bond of the sp^3-hybridized carbon, C-O bond, C&9552;O bond, and carbonate bond, respectively [33,34]. Among them, the intensity area ratios of the C&9552;C and C-C bonds (~80%) are higher than those of the other carbon bonds. This means that the carbon shell on the TiO_2 surface consists entirely of graphitic-like carbon. Furthermore, the XPS spectra and fitting curves of Ti 2p, C 1s, and O 1s suggest that the Ti-O-C bond is present, which is formed from the perfect contact between the TiO_2 core and graphitic-like carbon shell [35].

The nature of the carbon formed in the TiO_2@C-700 nanostructure was investigated by Raman spectroscopy, as shown in Fig. 5. The spectrum of the TiO_2@C-700 nanostructure shows two Lorentzian peaks around 1349~1356 and 1583–1596 cm^{-1}. The Raman-active E_{2g} mode at 1596 cm^{-1} is characteristic of graphitic sheets. The well-defined G-band for the TiO_2@C-700 nanostructure confirms the presence of sp^2-hybridized graphitic carbon structures within the carbonaceous layers. The D-band at around 1341 cm^{-1} can be attributed to the presence of defects within the hexagonal graphitic structure, and implies the presence of sp^3-hybridized carbon. Typically, the intensity ratio of the D-band to G-band of amorphous carbon (e.g., carbon black) is ~0.59 [36]. However, that of the TiO_2@C-700 nanostructure is ~0.80. By comparing the TEM, XPS, and Raman data of the TiO_2@C-700 nanostructure, it can be inferred

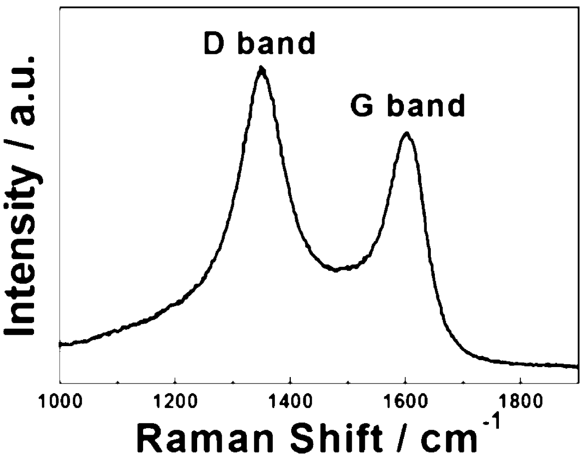

Fig. 5. Raman spectrum of the TiO_2@C-700 nanostructure.

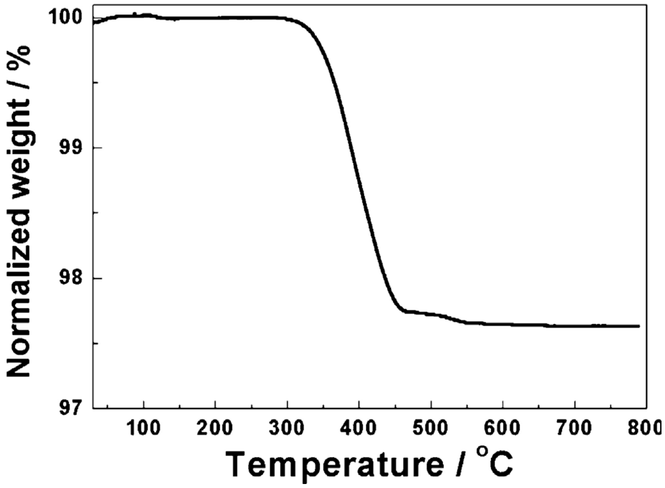

Fig. 6. TGA curve of the TiO_2@C-700 nanostructure in the range of 25–800 °C with a heating rate of 10 °C min^{-1} in an air flow of 60 cm^3 min^{-1}.

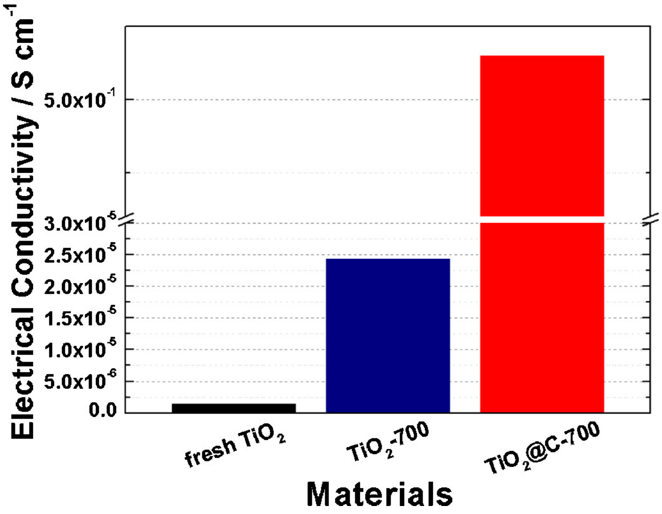

Fig. 7. Electrical conductivity of the fresh TiO_2 (Degussa Co.), TiO_2-700, and TiO_2@C-700 nanostructures. nanostructures.

that it consists of well-defined core-shell nanostructures comprising a TiO_2 core and graphitic-like carbon shell. Fig. 6 shows the TGA curve of the TiO_2@C-700 nanostructure in the range of 30–800 °C in an air flow. The normalized weight reduction of the TiO_2@C-700 nanostructure is ~2.4 wt.%, which is dominantly attributed to the oxidation of the graphitic-like carbon shell.

Fig. 7 shows a comparison of the electrical conductivity of the as-prepared samples. The fresh TiO_2 used as the starting material appears to have an extremely low electrical conductivity (1.37×10^{-6} S cm^{-1}). The electrical conductivity of the TiO_2-700 nanostructure formed through the heat treatment process for 3 h at 700 °C under an air atmosphere is 2.43×10^{-5} S cm^{-1}. On the other hand, the electrical conductivity of the TiO_2@C-700 nanostructure is $10^5 \sim 10^6$ times higher (0.65 S cm^{-1}) than those of the other samples and is similar to that of carbon black (Vulcan XC-72, 1.07 S cm^{-1}). The improved electrical conductivity of the TiO_2@C nanostructure may be due to its graphitic-like carbon shell, as compared to the TiO_2-700 nanostructure having semiconductor properties.

Fig. 8(a) and (b) show the charge/discharge curves of the TiO_2-700 and TiO_2@C-700 nanostructures, respectively, obtained at a current density of 0.2 C between 1 and 3 V. The first discharge curves of both samples show three plateau regions at around 1.75, 1.4, and 1.25 V. These three plateau regions are typically attributed to the anatase and rutile phases of the TiO_2 structure. The first plateau region at around 1.75 V is attributed to the phase transition between the tetragonal and orthorhombic phases with Li intercalation on the anatase phase of the TiO_2 structure [37,38]. The second and third plateau regions are attributed to structural rearrangement during lithium ion intercalation on the rutile phase of the TiO_2 structure from the original rutile *P4$_2$/mnm* to its lithiated form *P2/m* at 1.4 V and finally to a layered structure at 1.25 V [18,39–41]. At a cycling rate of 0.2 C, the first charge capacities of the TiO_2@C-700 and TiO_2-700 nanostructures are

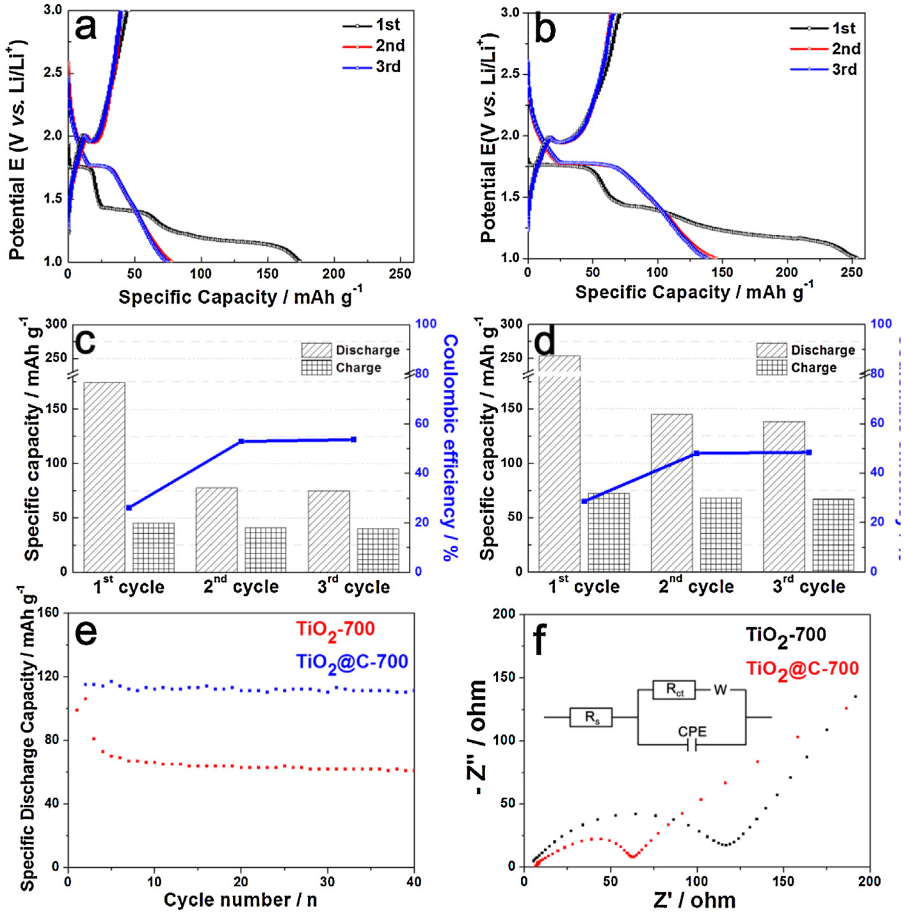

Fig. 8. Charge/discharge curves of (a) TiO_2-700 and (b) TiO_2@C-700 nanostructures at a current density of 0.2 C. Specific charge/discharge capacity and coulombic efficiency of (c) TiO_2-700 and (d) TiO_2@C-700 at 1st, 2nd, and 3rd cycles. (e) Cycling performance of the TiO_2-700 and TiO_2@C-700 nanostructures at 0.2 C for 40 cycles. (f) Nyquist plots of impedance data of the TiO_2-700 and TiO_2@C-700 nanostructures in the frequency range between 0.01 Hz and 100 kHz.

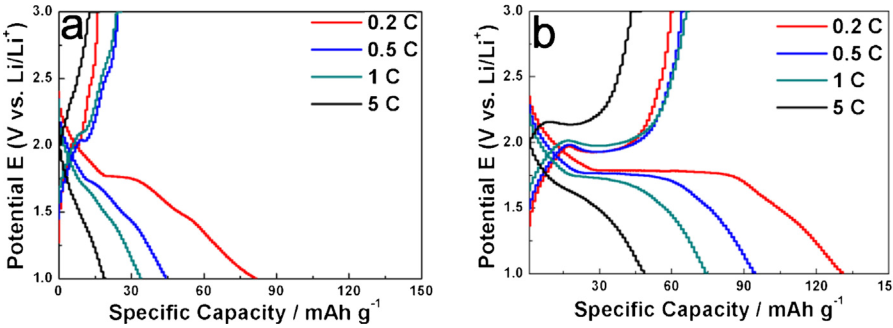

Fig. 9. The charge-discharge curves of (a) TiO_2-700 and (b) TiO_2@C-700 nanostructures at different C-rates from 0.5 to 5 C between 1 and 3 V.

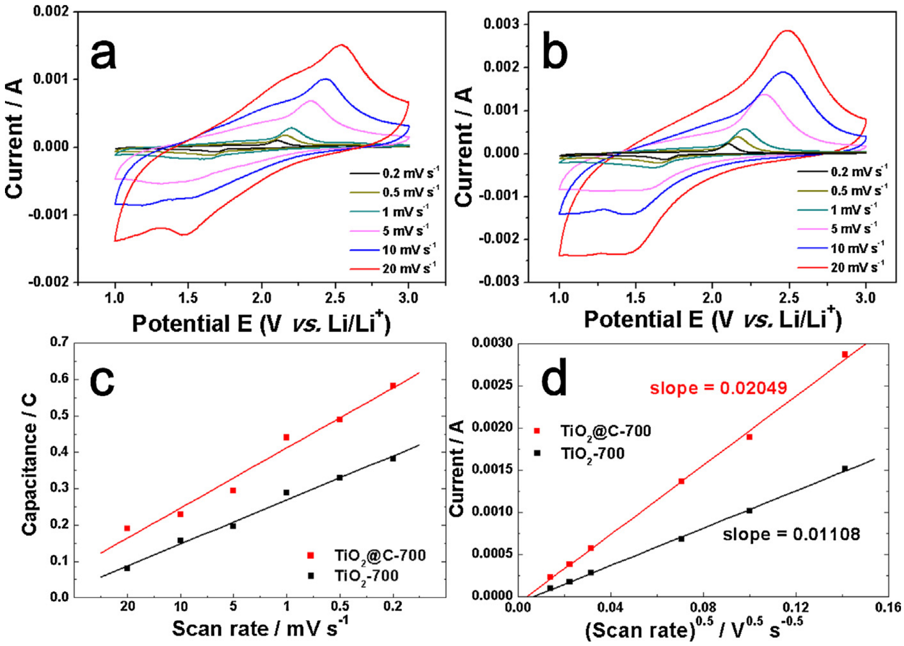

Fig. 10. CVs of (a) TiO_2-700 and (b) TiO_2@C-700 nanostructures at different scan rates between 0 and 3 V. (c) Specific capacity plots and (d) specific current plots of the charge potential in Fig. 5(a and b) as a function of the scan rates of the TiO_2-700 and TiO_2@C-700 nanostructures.

253 and 174 mAh g^{-1}, respectively. The second charge capacities of the TiO_2@C-700 and TiO_2-700 nanostructures are 145 and 77 mAh g^{-1}, respectively, representing irreversible intercalation properties. However, the low coulombic efficiency of the as-prepared electrodes can result from phase transition from rutile to spinel and then rock salt and small particle size (Fig. 8(c) and (d)). However, to design a full-cell battery configuration, the efficiency of the electrodes through an optimized nanostructure should be

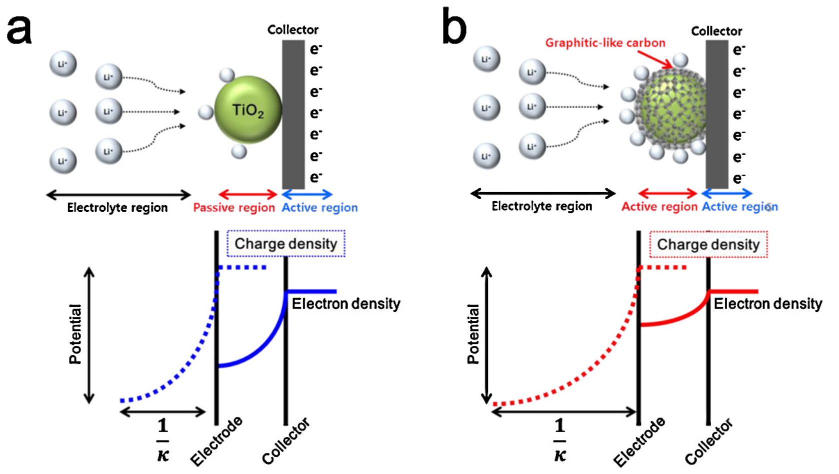

Fig. 11. Relationship between interface capacitance and electron density characteristics of (a) TiO_2-700 and (b) TiO_2@C-700 nanostructures according to Stern model.

improved. The cycling performance of the TiO_2@C-700 and TiO_2-700 nanostructures at a current rate of 0.2 C is indicated in Fig. 8(e). The TiO_2@C-700 nanostructure has much improved performance up to 40 cycles with a reversible capacity of 111 mAh g^{-1}, compared to that of the TiO_2-700 nanostructure (61 mAh g^{-1}). The capacity of the TiO_2@C-700 nanostructure (48.4 mAh g^{-1}) is 2.56 times higher than that of the TiO_2-700 nanostructure (18.9 mAh g^{-1}) at a high rate of 5 C. To further understand the improved specific discharge capacity of the TiO_2-700@C nanostructure, the Nyquist plots of the TiO_2@C-700 and TiO_2-700 nanostructures were obtained in the range between 100 kHz and 10 mHz after five cycles of charge/discharge, as shown in Fig. 8(f). The equivalent circuit was measured from the electrochemical impedance spectra in the inset of Fig. 8(f). The value of the diameter of the semicircle on the Z_{real} axis is related to the charge transfer resistance (R_{ct}) [42]. The values of R_{ct} of the TiO_2@C-700 and TiO_2-700 nanostructures are 56.6 and 111.4 Ω, respectively, indicating the much improved charge transport properties of the TiO_2@C-700 nanostructure due to its high electrical conductivity. The graphitic-like carbon shell acts as a conductive region, which improves the electron transport properties on the electrode surface and stabilizes its electronic and ionic conductivity, thereby lowering the charge transfer resistance.

As the C-rate increases from 0.2 to 5 C (Fig. 9), the specific discharge capacity of the lithium ions in the TiO_2@C-700 nanostructure remains higher than that of the TiO_2-700 nanostructure at all C-rates. The improved specific discharge capacity of the TiO_2@C-700 nanostructure cannot be due to the lithium intercalation capacity of the graphitic-like carbon shell, because the lithium ion intercalation in carbon-based anodic materials occurs between 0 and 1.0 V. However, the graphitic-like carbon shell with high electrical conductivity can increase the capacitance at the interface between the electrolyte and electrode. To evaluate the electrochemical properties of the TiO_2@C-700 and TiO_2-700 nanostructures, the CVs were obtained at different scan rates in the range from 0.2 to 20 mV s^{-1} after activation at 0.2 mV s^{-1} for three cycles, as shown in Fig. 10(a) and (b). As the scanning rate increases from 0.2 to 20 mV s^{-1} (Fig. 10(c)), the capacity of lithium ion intercalation of the TiO_2@C-700 nanostructure remains higher than that of the TiO_2-700 nanostructure at all scan rates. At a scan rate of 0.2 mV s^{-1}, the TiO_2@C-700 nanostructure (583.2 mC) exhibits a 1.52 times higher capacity than that of the TiO_2-700 nanostructure (382.5 mC). This outcome can be explained by the fact that the TiO_2@C-700 nanostructure has a fast diffusion rate during lithium ion intercalation and high capacitance, due to the graphitic-like carbon shell with its high electrical conductivity. Fig. 10(d) shows the relationship of the maximum peak current in the charge curve and the square root of the scan rate for the as-prepared nanostructures. The linear relationship between the peak current and square root of the scan rate demonstrates the diffusion limitation of the lithium ion intercalation, which is related to the behavior of the lithium ion insertion/desertion reaction [43,44]. The intercalation rate of lithium ions on an anode can be explained by their diffusion coefficient (D_{Li}). The diffusion coefficient was calculated using the Randles–Sevcik equation (3) as follows [45]:

$$I_p = 2.69 \times 10^5 n^{3/2} A D_{Li}^{1/2} C_{Li}^{*} \upsilon^{1/2} \qquad (3)$$

where I_P is the peak current, n is the number of electrons assuming a reaction electron number of 0.5 for typical TiO_2, A is the area of the electrode, C_{Li}^{*} is the bulk concentration of lithium ions in the electrode, and υ is the scan rate. The slopes of the linear curves for the TiO_2@C-700 and TiO_2-700 nanostructures are 0.02049 and 0.01108, respectively. The diffusion coefficients of lithium ions calculated from the slopes are 2.1×10^{-8} and 0.6×10^{-8} $cm^2 s^{-1}$ for the TiO_2@C-700 and TiO_2-700 nanostructures, respectively. This outcome is explained by the high diffusion coefficient of the TiO_2@C-700 nanostructure due to its high electrical conductivity.

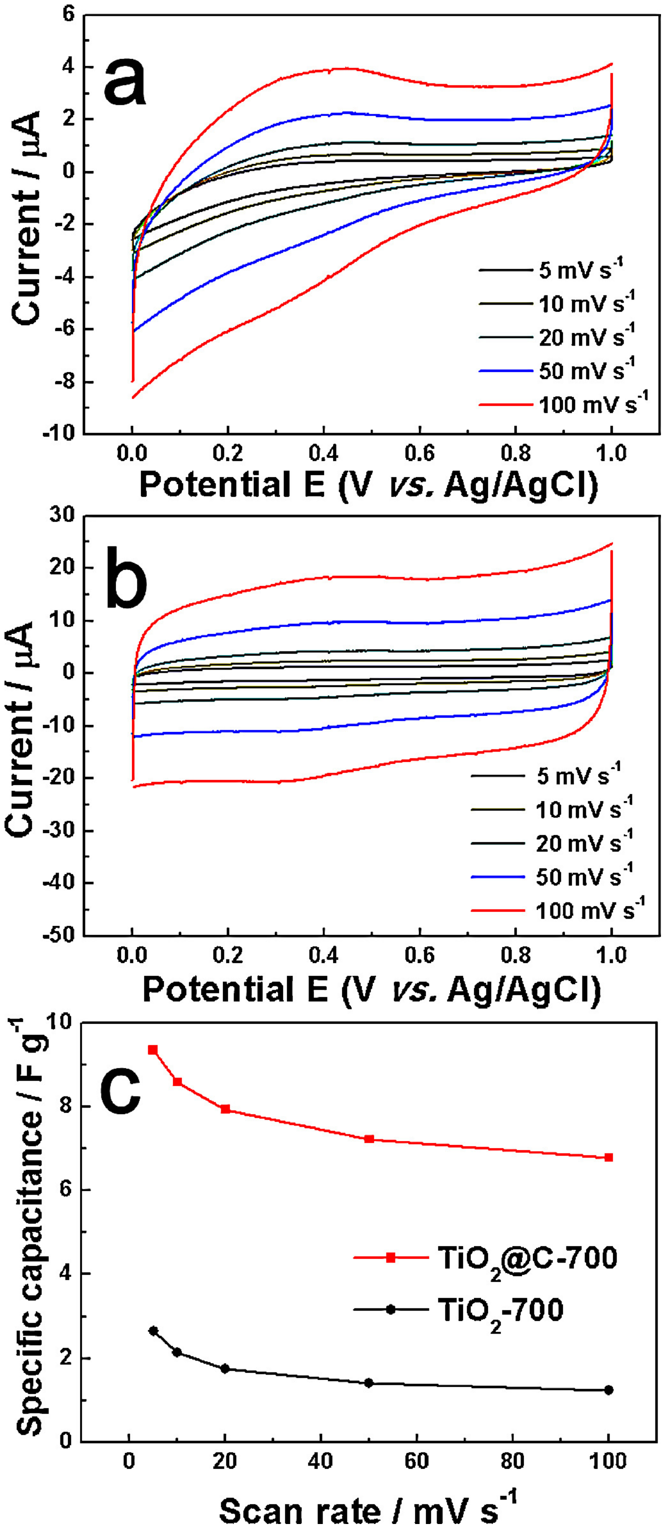

Fig. 12. CVs of (a) TiO_2-700 and (b) TiO_2@C-700 nanostructures at different scan rates between 0 and 1 V in 0.5 M H_2SO_4 solution at 25 °C. (c) Specific capacitance of the TiO_2-700 and TiO_2@C-700 nanostructures as a function of the scan rate.

According to Fig. 11, the improved lithium ion intercalation of the TiO_2@C-700 nanostructure can be explained by the basic principles of electrochemical storage, namely the functions of capacitor and battery. The graphitic-like carbon shell of the

TiO_2@C-700 nanostructure with its high electrical conductivity leads to a higher electron density on the active electrode in comparison with the TiO_2-700 nanostructure. Furthermore, the enhanced electron density on the active electrode may induce the wide electrical double layer required for achieving a high charge density. In the case of capacitor applications, a wide electrical double layer means a low interface resistance. According to the Debye-Huckel theory, the electric double layer is approximated to a diffusion double layer 1/k [46]. The electrode with high electrical conductivity shows an improved electric double layer and enhanced specific capacitance. Theoretically, the conducting electrode can have a high electron density between the electrode and collector, and induce a high lithium ion density at the interface. These electrical properties may give rise to a high lithium intercalation capacity and high-rate performance in LIBs. Thus, the TiO_2@C-700 nanostructure having high electrical conductivity would be expected to have a wider electrical double layer and enhanced specific capacitance in comparison with the TiO_2-700 nanostructure.

To estimate the capacitance of the TiO_2@C-700 and TiO_2-700 nanostructures, their CVs were measured at different scan rates between 0 and 1 V in 0.5 M H_2SO_4 solution using a potentiostat, as shown in Fig. 12(a) and (b). To estimate the specific capacitances at the interfaces between the electrode and electrolyte, 0.5 M H_2SO_4 solution containing hydrogen ions was selected as the electrolyte, because the CV performance in a non-aqueous electrolyte containing lithium ions incorporates the intercalation behavior of the lithium ion. At 50 $mV\,s^{-1}$, the TiO_2@C-700 nanostructure (7.22 $F\,g^{-1}$) exhibits a 4.13 times higher specific capacitance in comparison with the TiO_2-700 nanostructure (1.40 $F\,g^{-1}$), as shown in Fig. 12(a and b). When the scanning rate is increased from 5 to 100 $mV\,s^{-1}$ (Fig. 12(c)), the specific capacitances of the TiO_2@C-700 nanostructure are higher than those of the TiO_2-700 nanostructure at all scan rates. Furthermore, the TiO_2@C-700 nanostructure exhibits a CV with a rectangular shape, which means that it should have a low interface resistance in capacitor applications. Thus, the excellent lithium ion intercalation properties of the TiO_2@C-700 nanostructure may be attributed to its high electrical conductivity, improved interface capacitance, and low interface resistance in comparison with the TiO_2-700 nanostructure.

4. Conclusions

We reported the use of a complex nanostructure consisting of a TiO_2 core and carbon shell as the anodic materials for LIBs. The TiO_2@C nanostructure was successfully synthesized by a heating process under a CH_4 atmosphere at 700 °C. The TiO_2@C-700 nanostructure having a graphitic-like carbon shell shows improved electrical conductivity. The improved specific capacity and electrochemical properties of the TiO_2@C nanostructure are attributed to its graphitic-like carbon which acts as a conductive region affording improved electron transport properties on the electrode surface and enhanced lithium ion intercalation, thus leading to lower charge transfer resistance and high diffusion coefficient. Thus, by combining the electrochemical data and structural analysis, it can be concluded that the TiO_2@C nanostructure is a promising anode candidate for LIBs. However, the efficiency of the electrodes through an optimized nanostructure should be improved.

Conflict of interest

The authors declare no competing financial interest.

Acknowledgment

This research was supported by Basic Science Research Program through the National Research Foundation of Korea (NRF) funded by the Ministry of Education (NRF-2013R1A1A2012541) and the Human Resources Development program (No. 20124030200070) of the Korea Institute of Energy Technology Evaluation and Planning (KETEP) grant funded by the Korea government Ministry of Trade, Industry and Energy.

References

[1] H. Wang, D. Ma, X. Huang, Y. Huang, X. Zhang, General and Controllable Synthesis Strategy of Metal Oxide/TiO_2 Hierarchical Heterostructures with Improved Lithium-Ion Battery Performance, Sci. Rep. 2 (2012) 701.
[2] F.-M. Wang, M.-H. Yu, Y.-J. Hsiao, Y. Tsai, B.-J. Hwang, Y.-Y. Wang, C.-C. Wan, Aging Effects to Solid Electrolyte Interface (SEI) Membrane Formation and the Performance Analysis of Lithium Ion Batteries, Int. J. Electrochem. Sci. 6 (2011) 1014.
[3] S. Lee, H.-S. Kim, T.-Y. Seong, Electrochemical Properties of the Carbon-coated Lithium Vanadium Oxide Anode for Lithium Ion Batteries, J. Alloy. Compd. 509 (2011) 3136.
[4] H. Yang, T. Song, S. Lee, H. Han, F. Xia, A. Devadoss, W. Sigmund, U. Paik, Tin Indium Oxide/Graphene Nanosheet Nanocomposite as an Anode Material for Lithium Ion Batteries with Enhanced Lithium Storage Capacity and Rate Capability, Electrochem. Acta 91 (2013) 275.
[5] S. Yang, X. Zhou, J. Zhang, Z. Liu, Morphology-Controlled Solvothermal Synthesis of $LiFePO_4$ as a Cathode Material for Lithium-Ion Batteries, J. Mater. Chem. 20 (2010) 8086.
[6] B.-M. Hwang, S.-J. Kim, Y.-W. Lee, B. Han, S.-B. Kim, W.-S. Kim, K.-W. Park, Mesoporous Spinel $LiMn_2O_4$ Nanomaterial as a Cathode for High-Performance Lithium Ion Batteries, Int. J. Electrochem. Sci. 7 (2013) 9449.
[7] F. Wu, G. Tan, R. Chen, L. Li, J. Xiang, Y. Zheng, Novel Solid-State Li/$LiFePO_4$ Battery Configuration with a Ternary Nanocomposite Electrolyte for Practical Applications, Adv. Mater. 23 (2011) 5081.
[8] S.-J. Kim, Y.-W. Lee, S.-B. Han, S.-B. Kin, W.-S. Kim, K.-W. Park, Highly Improved Electrochemical Reactions of Mesoporous Carbon Electrodes in Electrochemical Energy Storage and Conversion, Int. J. Electrochem. Sci. 8 (2013) 3825.
[9] J. Chen, Y. Liu, A.I. Minett, C. Lynam, J. Wang, G.G. Wallace, Flexible Aligned Carbon Nanotube/Conducting Polymer Electrodes for a Lithium-Ion Battery, Chem. Mater. 19 (2007) 3595.
[10] A.L.M. Reddy, A. Srivastava, S.R. Gowda, H. Gullapalli, M. Dubey, P.M. Ajayan, Synthesis Of Nitrogen-Doped Graphene Films For Lithium Battery Application, ACS Nano 4 (2010) 6337.
[11] H. Li, T. Zhai, P. He, Y. Wang, E. Hosono, H. Zhou, Single-Crystal $H_2V_3O_8$ Nanowires: a Competitive Anode with Large Capacity for Aqueous Lithium-Ion Batteries, J. Mater. Chem. 21 (2011) 1780.
[12] M.H. Oh, T. Yu, S.-H. Yu, B. Lim, K.-T. Ko, M.-G. Willinger, D.-H. Seo, B.H. Kim, M. G. Cho, J.-H. Park, K. Kang, Y.-E. Sung, N. Pinna, T. Hyeon, Galvanic Replacement Reactions in Metal Oxide Nanocrystals, Science 340 (2013) 964.
[13] H. Wang, L.-F. Cui, Y. Yang, H.S. Casalongue, J.T. Robinson, Y. Liang, Y. Cui, H. Dai, Mn_3O_4-Graphene Hybrid as a High-Capacity Anode Material for Lithium Ion Batteries, J. Am. Chem. Soc. 132 (2010) 13978.
[14] J.-Z. Md.M. Rahman, Wang, M.F. Hassan, D. Wexler, H.K. Liu, Amorphous Carbon Coated High Grain Boundary Density Dual Phase $Li_4Ti_5O_{12}$-TiO_2: A Nanocomposite Anode Material for Li-Ion Batteries, Adv. Energy Mater. 1 (2011) 212.
[15] J.W. Kang, D.H. Kim, V. Mathew, J.S. Kim, J.H. Gim, J. Kim, Particle Size Effect of Anatase TiO_2 Nanocrystals for Lithium-Ion Batteries, J. Electrochem. Soc. 158 (2011) A59.
[16] S. Liu, Z. Wnag, C. Yu, H.B. Wu, G. Wang, Q. Dong, J. Qiu, A. Eychmüller, X.W. Lou, A Flexible TiO_2(B)-Based Battery Electrode with Superior Power Rate and Ultralong Cycle Life, Adv. Mater. 25 (2013) 3462.
[17] H. Park, T. Song, H. Han, A. Devadoss, J. Yuh, C. Choi, U. Paik, SnO_2 Encapsulated TiO_2 Hollow Nanofibers as Anode Material for Lithium Ion Batteries, Electrochem. Commun. 22 (2012) 81.
[18] D. Dambournet, I. Belharouak, K. Amine, Tailored Preparation Methods of TiO_2 Anatase Rutile, Brookite: Mechanism of Formation and Electrochemical Properties, Chem. Mater. 22 (2010) 1173.
[19] A.G. Dylla, G. Henkelman, K.J. Stevenson, Lithium Insertion in Nanostructured TiO_2(B) Architectures, Accounts Chem. Res. 46 (2013) 1104.
[20] A.K. Rai, L.T. Anh, J. Gim, V. Mathew, J. Kang, B.J. Paul, J. Song, J. Kim, Simple Synthesis and Particle Size Effects of TiO_2 Nanoparticle Anodes for Rechargeable Lithium Ion Batteries, Electrochim. Acta 90 (2013) 112.
[21] Z. Wang, X.W. Lou, TiO_2 Nanocages: Fast Synthesis Interior Functionalization and Improved Lithium Storage Properties, Adv. Mater. 24 (2012) 4124.
[22] H. Kim, M.G. Kim, J. Cho, Unique Structural Changes of Three-Dimensionally Ordered Macroporous TiO_2 Electrode Materials During Electrochemical Cycling, Adv. Energy Mater. 2 (2012) 1425.
[23] B. Han, S.-J. Kim, B.-M. Hwang, E.-T. Hwang, H.-C. Park, M.-H. Koh, K.-W. Park, TiO_2 Branched Nanostructure Anode Material Prepared by Seeding Method for

High-performance Lithium Ion Batteries, J. Korean Electrochem. Soc. 6 (2013) 81.

[24] A. Lamberti, N. Garino, A. Sacco, S. Bianco, D. Manfredi, C. Gerbaldi, Vertically Aligned TiO_2 Nanotube Array for High Rate Li-based Micro-Battery Anodes with Improved Durability, Electrochim. Acta 102 (2013) 233.

[25] C. Lai, G.R. Li, Y.Y. Dou, X.P. Gao, Mesoporous Polyaniline or Polypyrrole/Anatase TiO_2 Nanocomposite as Anode Materials for Lithium-Ion Batteries, Electrochim. Acta 55 (2010) 4567.

[26] C. Lai, H.Z. Zhang, G.R. Li, X.P. Gao, Mesoporous Polyaniline/TiO_2 Microspheres with Core–Shell Structure as Anode Materials for Lithium Ion Battery, J. Power Sources 196 (2011) 4735.

[27] Z. Yang, G. Du, Q. Meng, Z. Guo, X. Yu, Z. Chen, T. Guo, R. Zeng, Synthesis of Uniform TiO_2@Carbon Composite Nanofibers as Anode for Lithium Ion Batteries with Enhanced Electrochemical Performance, J. Mater. Chem. 22 (2012) 5848.

[28] Z. Yang, G. Du, Z. Guo, X. Yu, Z. Chen, T. Guo, H. Liu, TiO_2(B)@Carbon Composite Nanowires as Anode for Lithium Ion Batteries with Enhanced Reversible Capacity and Cyclic Performance, J. Mater. Chem. 21 (2011) 8591.

[29] Z. Yang, Q. Meng, Z. Guo, X. Yu, T. Guo, R. Zeng, Highly Uniform TiO_2/SnO_2/Carbon Hybrid Nanofibers with Greatly Enhanced Lithium Storage Performance, J. Mater. Chem. A 1 (2013) 10395.

[30] J. Ovenston, K. Wanagisawa, Effect of Hydrothermal Treatment of Amorphous Titania on the Phase Change from Anatase to Rutile during Calcination, Chem. Mater. 11 (1999) 2770.

[31] D.A.H. Hanaor, C.C. Sorrell, Review of the Anatase to Rutile Phase Transformation, J. Mater. Sci. 46 (2011) 855.

[32] G. An, W. Ma, Z. Sun, Z. Liu, B. Han, S. Miao, Z. Miao, K. Ding, Preparation of Titania/Carbon Nanotube Composites using Supercritical Ethanol and Their Photocatalytic Activity for phenol Degradation under Visible Light Irradiation, Carbon 45 (2007) 1795.

[33] L.-W. Zhang, G.-B. Fu, Y.-F. Zhu, Efficient TiO_2 Photocatalysts from Surface Hybridization of TiO_2 Particles with Graphite-like Carbon, Adv. Funct. Mater. 18 (2008) 2180.

[34] T. Hyeon, S. Han, Y.-E. Sung, K.-W. Park, Y.-W. Kim, High-Performance Direct Methanol Fuel Cell Electrodes using Solid-Phase-Synthesized Carbon Nanocoils, Angew. Chem. Int. Ed. 42 (2003) 4352.

[35] Y. Cong, X. Li, Y. Qin, Z. Dong, G. Yuan, Z. Cui, X. Lai, Carbon-doped TiO_2 Coating on Multiwalled Carbon Nanotubes with Higher Visible Light Photocatalytic Activity, Appl. Catal. B-nviron. 107 (2011) 128.

[36] S. Hussain, R. Amade, E. Jover, E. Bertran, Functionalization of Carbon Nanotubes by Water Plasma, Nanotechnology 23 (2012) 385604.

[37] D. Wang, D. Choi, J. Li, Z. Yang, Z. Nie, R. Kou, D. Hu, C. Wang, L.V. Saraf, J. Zhang, I.A. Aksay, J. Liu, Self-Assembled TiO_2–Graphene Hybrid Nanostructures for Enhanced Li-Ion Insertion, ACS Nano 3 (2009) 907.

[38] I. Moriguchi, R. Hidaka, H. Yamada, T. Kudo, H. Murakami, N. Nakashima, A Mesoporous Nanocomposite of TiO_2 and Carbon Nanotubes as a High-Rate Li-Intercalation Electrode Material, Adv. Mater. 18 (2006) 69.

[39] M. Vijayakumar, S. Kerisit, C. Wang, Z. Nie, K.M. Rosso, Z. Yang, G. Graff, J. Liu, J. Hu, Effect of Chemical Lithium Intercalation into Rutile TiO_2 Nanorods, J. Phys. Chem. C 113 (2009) 14567.

[40] W.J.H. Borghols, M. Wagemaker, U. Lafont, E.M. Kelder, F.M. Mulder, Impact of Nanosizing on Lithiated Rutile TiO_2, Chem. Mater. 20 (2008) 2949.

[41] E. Baudrin, S. Cassaignon, M. Koelsch, J.-P. Jolivet, L. Dupont, J.-M. Tarascon, Structural Evolution during the Reaction of Li with Nano-Sized Rutile Type TiO_2 at Room Temperature, Electrochem. Commun. 9 (2007) 337.

[42] B.-L. He, B. Dong, H.-L. Li, Preparation and Electrochemical Properties of Ag-Modified TiO_2 Nanotube Anode Material for Lithium–Ion Battery, Electrochem. Commun. 9 (2007) 425.

[43] L. Wang, X. Li, Z. Tang, X. Zhang, Pt Supported on Phosphorus-doped Carbon Nanotube as an Anode Catalyst for Direct Methanol Fuel Cells, Electrochem. Commun. 22 (2012) 73.

[44] S. Ni, T. Li, X. Lv, X. Yang, L. Zhang, Designed Constitution of NiO/Ni Nanostructured Electrode for High Performance Lithium Ion Battery, Electrochim. Acta 91 (2013) 267.

[45] Z. Zheng, Y. Wang, A. Zhang, T. Zhang, F. Cheng, Z. Tao, J. Chen, Porous Li_2FeSiO_4/C Nanocomposite as the Cathode Material of Lithium-Ion Batteries, J. Power Sources 198 (2012) 229.

[46] C.W. Outhwaite, L.B. Bhuiyan, Theory of the Electric Double Layer using a Modified Poisson–Boltzman Equation, J. Chem. Soc. Faraday Trans. 76 (1980) 1388.